Magnetic resonance imaging of a stream of bubbles injected into liquid suspensions

Alireza Bordbar[a*], Wasif Zia[b*], Janine Birnbaum[c], Javad Omidi[a], Ray F. Lee[d], Einat Lev[c], Christopher M. Boyce[a†]

[a]Department of Chemical Engineering, Columbia University, New York, NY, USA

[b]Nathan Kline Institute, Orangeburg, NY, USA

[c]Lamont-Doherty Earth Observatory, Columbia University, 61 Route 9W, Palisades, NY, USA

[d]Zuckerman Mind Brain Behavior Institute, Columbia University, New York, NY, USA

[*]these authors contributed equally to this work

[†]Corresponding author: cmb2302@columbia.edu

Abstract

Magnetic resonance imaging (MRI) is a powerful tool for characterizing opaque multiphase flows non-invasively. However, MRI has often (i) had low temporal resolution and thus not captured transient dynamics, (ii) only provided 2D slice images of 3D flows and (iii) been limited to flows in narrow (~30 mm) tubes with significant wall effects. Here, we apply multi-band echo planar imaging (MB-EPI) with a custom-built radiofrequency coil in a full-body MRI scanner to provide fully 3D images of the dynamics of a stream of bubbles rising through a dense suspension with 151 ms resolution in a 178 mm diameter system. Image processing demonstrates that bubble rise and coalescence dynamics vary significantly with (a) initial spacing between bubbles and (b) particle volume fraction. The ability to image bubble dynamics in dense suspensions as well as in full 3D provides future opportunities to characterize complex, non-axisymmetric, multiphase flows.

1. Introduction

Streams of gas bubbles are injected into and rise vertically through liquids and liquid-solid suspensions in a range of industrial and natural systems [1,2]. The ascent, coalescence, and splitting of these bubbles induce convection and mixing [3]. The rate and efficiency of mixing are controlled by the bubble properties and dynamics such as bubble size and rise velocity. In particle-bearing suspensions, the particles influence bubble dynamics, while in turn the bubbles also influence the convection and mixing of particles [4,5].

Bubble dynamics in clear fluids can be characterized using optical imaging [6,7]. However, particle-bearing suspensions are opaque, which precludes measurement of the bubble and suspension dynamics in flow interiors using optical imaging. Tomographic imaging, including X-ray, electrical capacitance tomography (ECT), positron emission particle tracking (PEPT), and magnetic resonance imaging (MRI), have been used to characterize bubbly flow dynamics in opaque fluids providing insights on single bubbles and bubble interaction, as well as gas, liquid and particle motion [8–26]. These measurements have been limited by the balance between spatial and temporal resolution which has made it very difficult to acquire images on a time-scale of milliseconds as needed to effectively capture the dynamics of bubble coalescence, while also capturing 3D images. Many studies have captured 2D slices through 3D opaque flows [27]; however, the complex and 3D dynamics in these systems make it such that 2D slice images do not provide the full set of insights into the flow.

Like other tomographic techniques, MRI can measure the contrast between gas and liquid to image the location of bubbles. In addition, MRI can measure the velocity of liquid, particles, and gas [28,29]. MRI has traditionally been limited in temporal resolution, and thus most studies have produced time-averaged measurements of void fraction and velocity field [30]. However, recent studies using Fast Low Angle Shot (FLASH) [31], echo planar imaging (EPI) [29] and ultrashort echo time (UTE) protocols [24] have allowed capturing 2D slices in just a few milliseconds. In medical imaging, Multi-band EPI (MB-EPI) is a recent technique that allows for rapid collection of 3D images through the acquisition of multiple closely spaced 2D slices that are stitched together [32].

Here, we utilize EPI and MB-EPI images to produce 2D and 3D images, respectively, of a stream of bubbles rising through suspensions of silicone oil and sesame seeds. The injection time of bubbles and the idle time between bubbles are varied, as well as the volume fraction of suspended solid particles to investigate the effects of these variables on bubble and particle dynamics. Our experiments demonstrate the capability of MRI to provide insights into the location and timing of bubble coalescence, as well as the mixing of elongated particles in dilute and concentrated suspensions.

2. Methods

In this experimental study, we study streams of bubbles within a medical MRI scanner by tailoring and implementing MRI techniques to study bubble dynamics, and reconstructing images and extracting bubble statistics from the measurements.

2.1 Flow Setup

A cylindrical container with an internal diameter of 178 mm, and a height of 400 mm was constructed from acrylic to be compatible with MRI (**Fig. 1**). At the center of the base of the container, a one-way valve was placed flush with the base to inject air bubbles into the system. An air supply at 5 psi (gauge) was used with a solenoid valve opened for an “injection time” during which bubbles were injected and then closed for an “idle time” between consecutive injections to form a stream of periodically injected bubbles. The container was filled with a combination suspension of 5000 cSt silicone oil with a density of 970 kg/m^3 and sesame seeds (long axis 3.1±0.3 mm, middle axis of 1.7±0.2 mm, and short axis of 0.6±0.2 mm (20 seeds sampled)) with a particle density of 1300 kg/m^3 to a height of 380 mm. The exact amount of oil and seeds added was varied to control the volume fraction of seeds in the suspension and measured by the weight of seeds and volume of liquid.

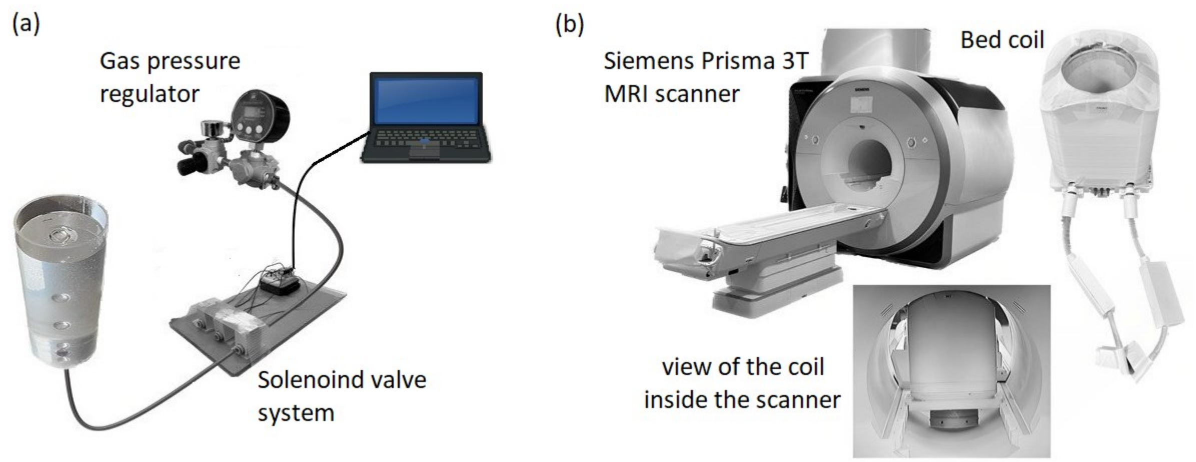

Fig. 1 Schematic of the flow setup: (a) flow setup and (b) MRI coil and scanner.

2.2 Magnetic Resonance Imaging (MRI)

MRI measurements were conducted tuned to ^{1}H nuclei which provided signal predominantly from the silicone oil, such that regions with high signal are indicative of the location of silicone oil and regions with low signal are indicative of regions with gas bubbles. Measurements were conducted on a 3T Siemens Prisma MRI scanner, with 16 receiving coils and a scanner frequency of 123.26 MHz. The use of multiple receiving coils allows for improved temporal resolution. An EPI [33] pulse sequence (**Fig. 2a**) (time coordinated sequences of radiofrequency (r.f.) pulses and magnetic field gradients) was used to acquire 2D slice images through a central vertical slice in the system with a temporal resolution of 58 ms, a horizontal and vertical resolution of 3.5 mm, and a slice thickness of 5 mm. EPI acquires an entire image from only one radiofrequency pulse to excite the spins in the sample, scanning through frequency space in a grid-like fashion, distinguishing EPI from other techniques which use multiple excitation points to sample frequency space and create an image. As such, EPI typically achieves a temporal resolution much faster than techniques often used to characterize multiphase flow, such as spin-warp imaging [34], single point imaging [35] and FLASH imaging [36]. The number of points acquired in the frequency-encoding direction was 80, and number of points acquired in the phase-encoding direction was 48 for the 2D scans, corresponding to a field-of-view (FoV) of 203 mm (horizontal) by 280 mm (vertical). The flip angle was 16 degrees. These values were chosen to balance the temporal resolution, spatial resolution and field-of-view to achieve resolution to characterize the bubbly flow of interest, since improving spatial resolution would come at the expense of temporal resolution and vice-versa.

For the 3D measurements, an MB-EPI [37] pulse sequence (**Fig. 2b**) was conducted with 12 slices through the system, taken with 2.5 mm spacing between slices, and 5 mm slice thickness. MB-EPI uses the sampling method of frequency space of EPI, but employs multiple excitation pulses directed at different slices through the sample to record 2D images of multiple slices in quick succession, which can be stitched together to form rapid 3D images. The temporal resolution of the 3D images was 151 ms, and the spatial resolution was 3.5 mm, with a field-of-view of 203 mm × 87.5 mm (horizontal), and 280 mm (vertical). The temporal and spatial resolution and number of slices again were selected to balance temporal and spatial resolution to be able to characterize the bubbly system studied here. **Fig. 3** shows how these 2D slices are positioned and stacked together to cover the space for 3D acquisitions. Experiments were conducted over the course of 90 s.

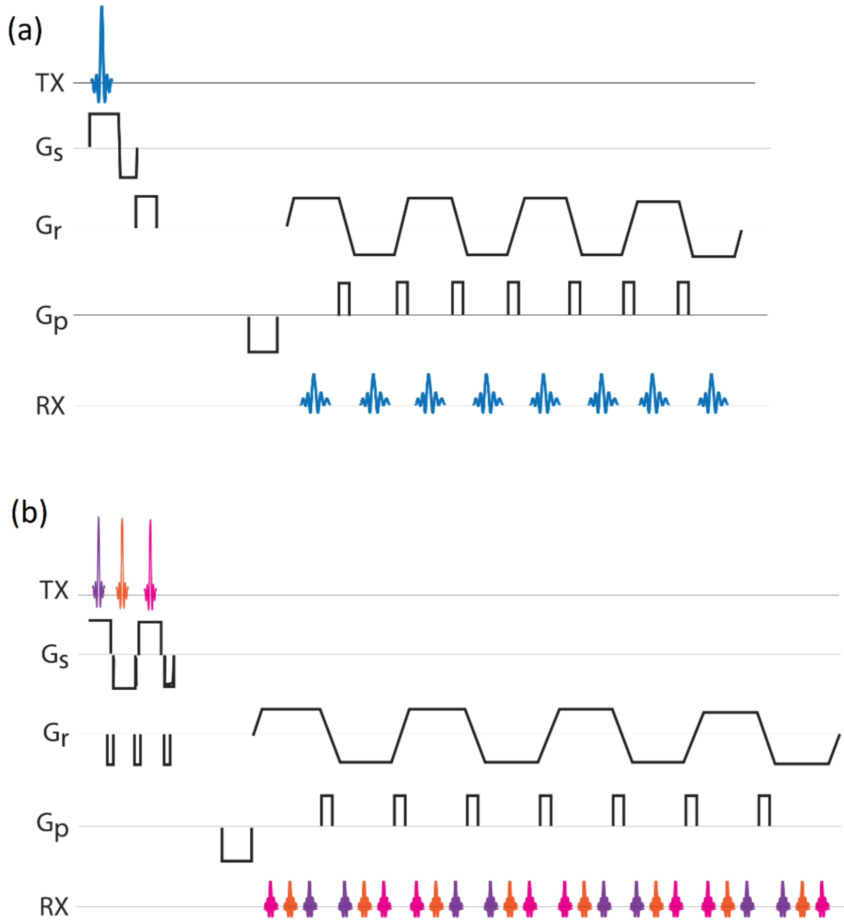

Fig. 2: Pulse sequence diagrams for the protocols used for rapid (a) 2D EPI and (b) 3D MB-EPI of bubble dynamics, adapted from [37]. The diagrams show the initial portion of the pulse sequences.

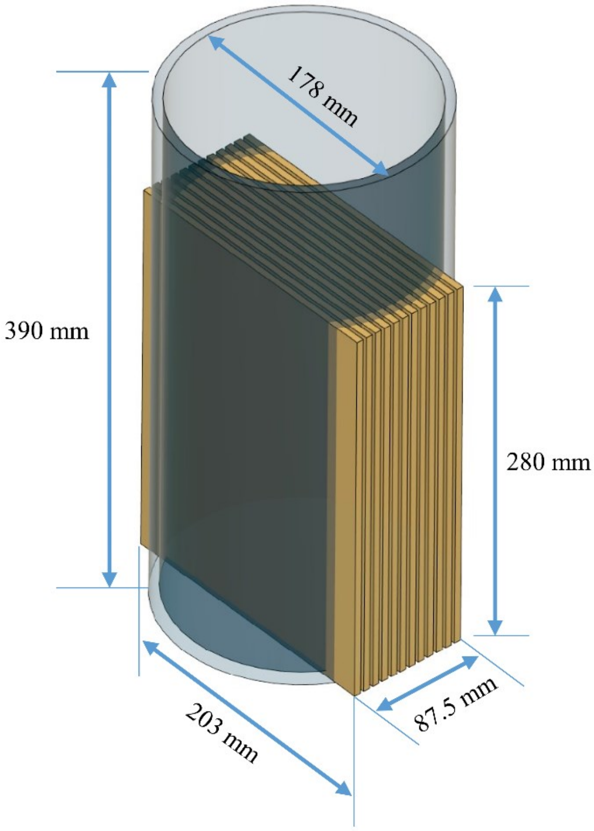

Fig. 3 Schematic of slice dimensions and positions in the 3D acquisitions,

2.3 Data Processing

Image processing was conducted using MATLAB and 3D Slicer to reconstruct MRI data to produce 2D and 3D images. The process starts with importing NIFTI (Neuroimaging Informatics Technology Initiative) image files obtained from the scanner into MATLAB. Then, using filters available in the Image Processing Toolbox, the image quality is enhanced. The filters used were *Imadjust* which adjusts the intensity values of the image, *medfilt2* which performs median filtering of the 2D image, *imgaussfilt* which applies Gaussian filtering, *imsharpen* which sharpens the image, *imbinarize* which binarizes the image, and finally, *bwareaopen* which removes small, connected components (objects) from the binarized image. The produced images from the process are later used to make time-series images for different cases (**Fig. 4a**). It must be noted that in all cases, the field-of-view of the images and the extracted regions of interest for filtering are the same. Varying filtering parameters, such as the signal threshold for binarization, was found to yield small quantitative differences in bubble area, but no significant differences in the center positions of bubbles or the bubble rise velocity.

From 2D images, we extracted bubble area, bubble rise velocity, and vertical bubble position over time. MATLAB image processing was used to determine the center of connected gas-phase pixels as the center of a bubble (**Fig. 4b**). The total area of all of the pixels in a binarized bubble was used to determine the bubble area. Two bubbles were considered to coalesce when the binarized gas-phase pixels from the bubbles became interconnected. As shown in **Fig. 4c** as a sample case, bubbles are numbered consecutively as they appear in the frame. However, immediately after the boundaries of two individual bubbles begin to touch, their IDs are replaced with a new bubble ID assigned to the newly formed bubble as a result of the coalescence process. In the case of 3D scans, multiple 2D slices with certain slice thickness and slice spacing are acquired. However, the temporal resolution and signal-to-noise ratio are poorer compared to single-slice 2D scans. In the future, the temporal resolution and signal-to-noise ratio could be improved by using an MRI scanner with a stronger field, stronger gradients, and a higher slew rate as well as a receiver coil specially designed for MB-EPI signal reception for the flow system of interest. Images were binarized using the same filtering process as with 2D images. 3D Slicer software [38] was used to make the 3D images from the binarized data files.

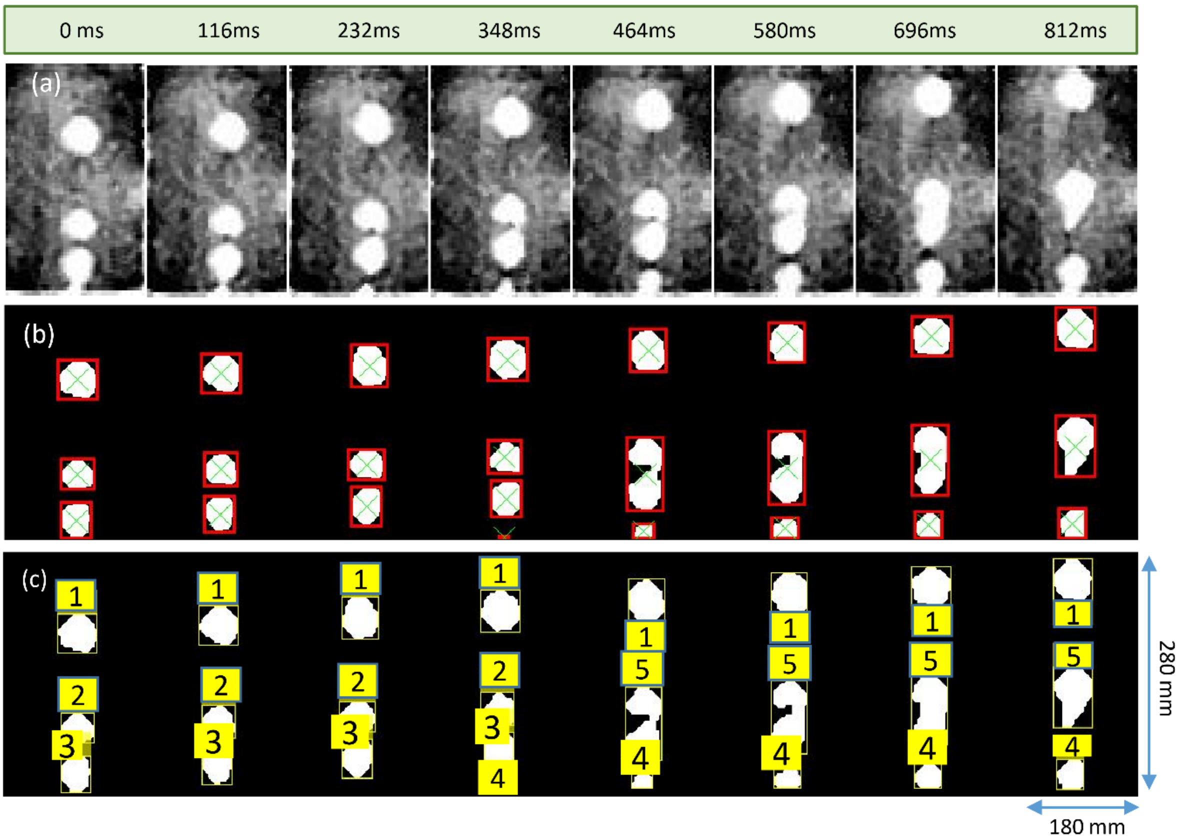

Fig. 4 (a) Raw 2D MRI data and (b) binarized data showing bubbles and liquids and marking the center of each bubble with × and the perimeter of each bubble in red and (c) binarized data showing how numbers are assigned to the injected and the newly formed coalesced bubbles.

3. Results and Discussion

We studied bubble rise dynamics across a range of conditions: (a) constant bubble injection conditions with varying volume fractions of suspended seeds (Section 3.1) and (b) varying idle time between bubble injections with (i) 20 vol% seeds (Section 3.2) and (ii) 40 vol% seeds (Section 3.3).

3.1 Varying Volume Fraction of Seeds

Fig. 5 shows time series of images (different rows showing different volume fractions of seeds) for bubble dynamics in a central vertical slice through the system with white indicating areas with bubbles and dark areas indicating areas of suspension. The time series are over the course of approximately four bubble injections with each bubble injection occurring every 860 ms, which is approximately every three image frames. Bubble size tends to increase with increasing vertical position in the cylinder due to bubble coalescence. The rate at which the highest bubble in the system rises over time tends to decrease with increasing volume fraction, which can be attributed to the increasing effective viscosity with increasing volume fraction of seeds [39].

Fig. 5 Time series of 2D central vertical slice images of bubble streams rising through suspensions with different volume fractions. Injection time: 160 ms; idle time: 700 ms. The timestamps are relative to the zero frame chosen for each case; the absolute times of the first tile on each row are 30.3 s, 20.2 s, 5.9 s, 50.3 s, and 80.6 s, respectively.

Fig. 6 shows 3D images of bubble dynamics in the 0% and 10% seeds cases. The images are cropped at the sides because the low signal-to-noise ratio sometimes produced erroneous bubbles in the side regions. Further, the 20% and higher volume fraction seeds cases are not shown because their signal-to-noise ratio was too low to produce accurate 3D images of bubbles. The 3D images show that the bubble shapes are not always axisymmetric, particularly at times surrounding bubble coalescence. This asymmetry can be attributed at least in part to the fact that the bubbles are rising through a suspension of non-spherical particles which the bubbles push and rearrange. The complex and often uneven nature of rearrangement of granular particles, particularly non-spherical grains, can potentially explain this asymmetry.

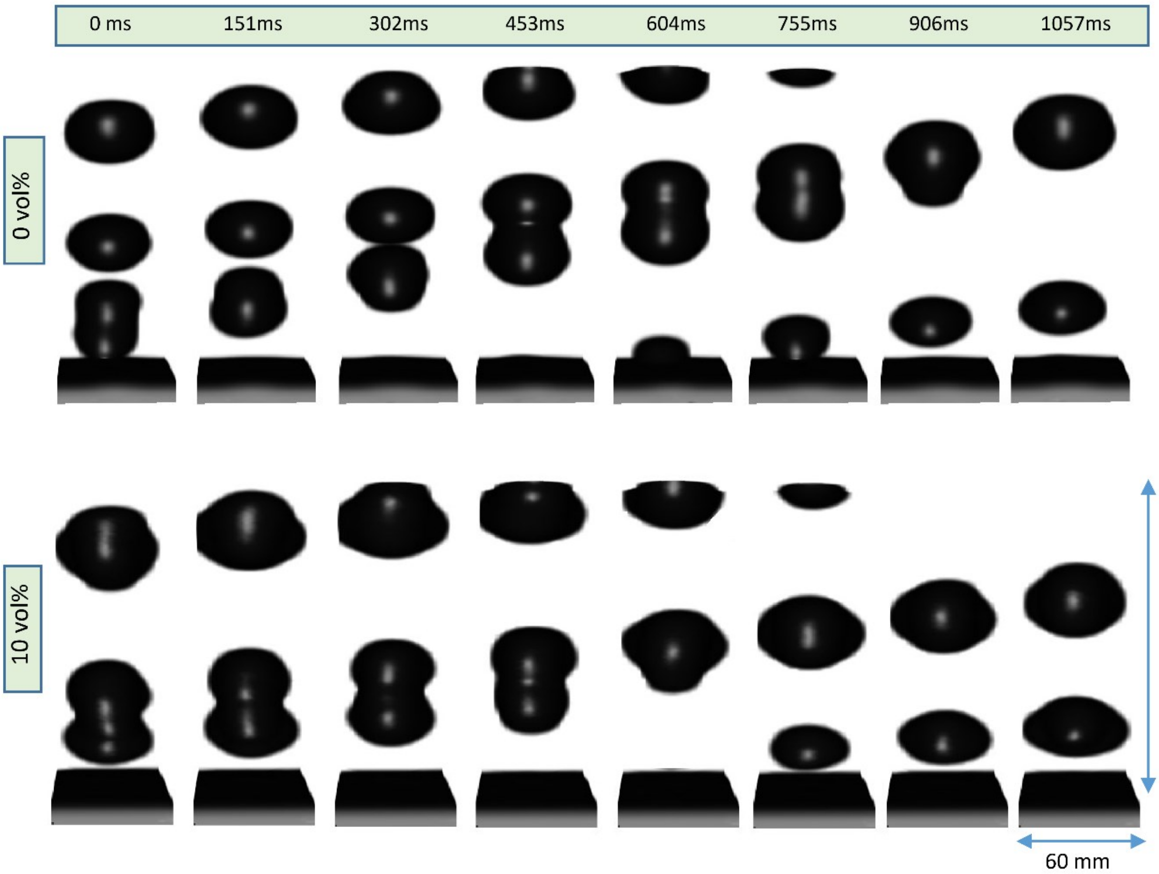

Fig. 6 Time series of 3D images of bubble streams rising through suspensions of 0% (top) and 10% (bottom) volume fraction of seeds with a constant injection time of 160 ms and idle time of 700 ms.

Fig. 7 shows the bubble trajectories vs. time with blue stars indicating points of bubble coalescence (left column) and corresponding vertical position vs. average bubble area (right column) for (a) 0%, (b) 10% and (c) 20% seeds based on processing the 2D images. In all cases, bubble coalescence occurs, causing the bubble area to increase with increasing vertical position. For the 0% and 10% cases, there is no clear trend to where coalescence occurs in the system, and as a result, the bubble area increases steadily with increasing vertical position. In the 20% case, bubble coalescence occurs between every two bubbles repeatedly at a vertical position of approximately 50 mm above the injection port. The periodic bubble coalescence in the 20% suspension leads to a sharp increase in bubble area at approximately 50 mm above the injection port, followed by a slight decrease in area as the coalesced bubbles adjust from an elongated to a spherical shape (consistent with a conservation of volume). The bubbles in the

0% case are significantly smaller than those in the 10% or 20% cases because the initial bubble often breaks into two during the injection.

Fig. 8 shows the probability density function of bubble area and the relationship between bubble velocities and bubble area for cases shown in **Fig. 7**. For the 20% volume case (e,f), a bimodal bubble area distribution is observed (e), and most bubbles are grouped in two velocity regions (f), corresponding to before and after coalescence. This binary grouping can be attributed to regular bubble coalescence. For the 0% and 10% cases, the distribution of the areas is more spread out due to the non-regularity of coalescence events, and the majority of the bubbles are smaller in size relative to the 20% case since fewer bubbles coalesce lower in the system because there are fewer particles to slow bubble rise. Bubbles rise with lower velocities as volume fraction is increased due to the increase in resistance to bubble motion with increasing particle concentration. In all cases, low velocity outliers can be attributed to bubbles apparently rising very slowly as two bubbles merge and the apparent rise velocity registered derives more from the shape adjustment than the merged bubble rising.

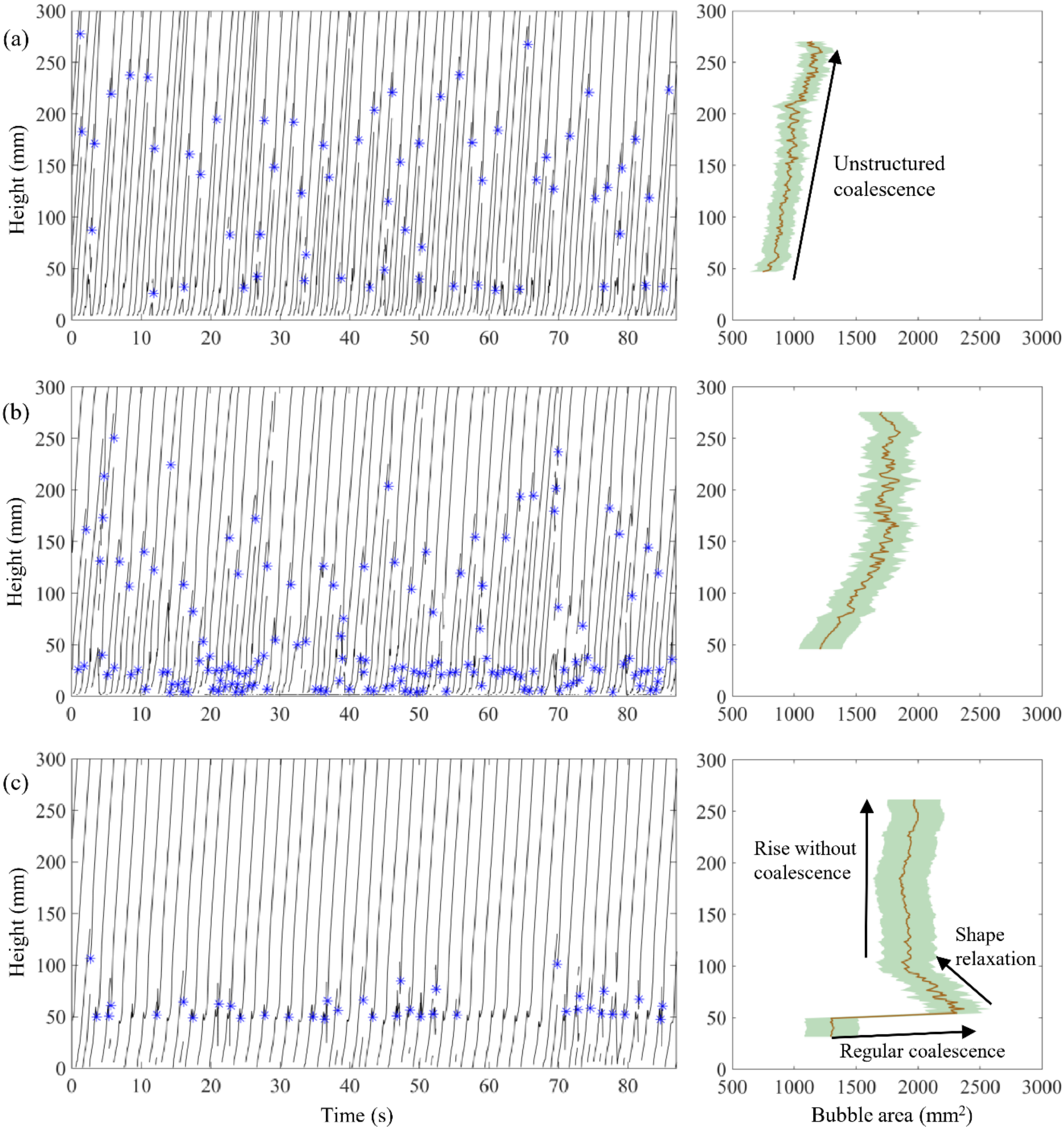

Fig. 7 Vertical bubble position vs. time (first column) and vs. bubble area (second column) with seed volume fractions of (a) 0%, (b) 10%, and (c) 20% with a constant injection time of 160 ms and idle time of 700 ms.

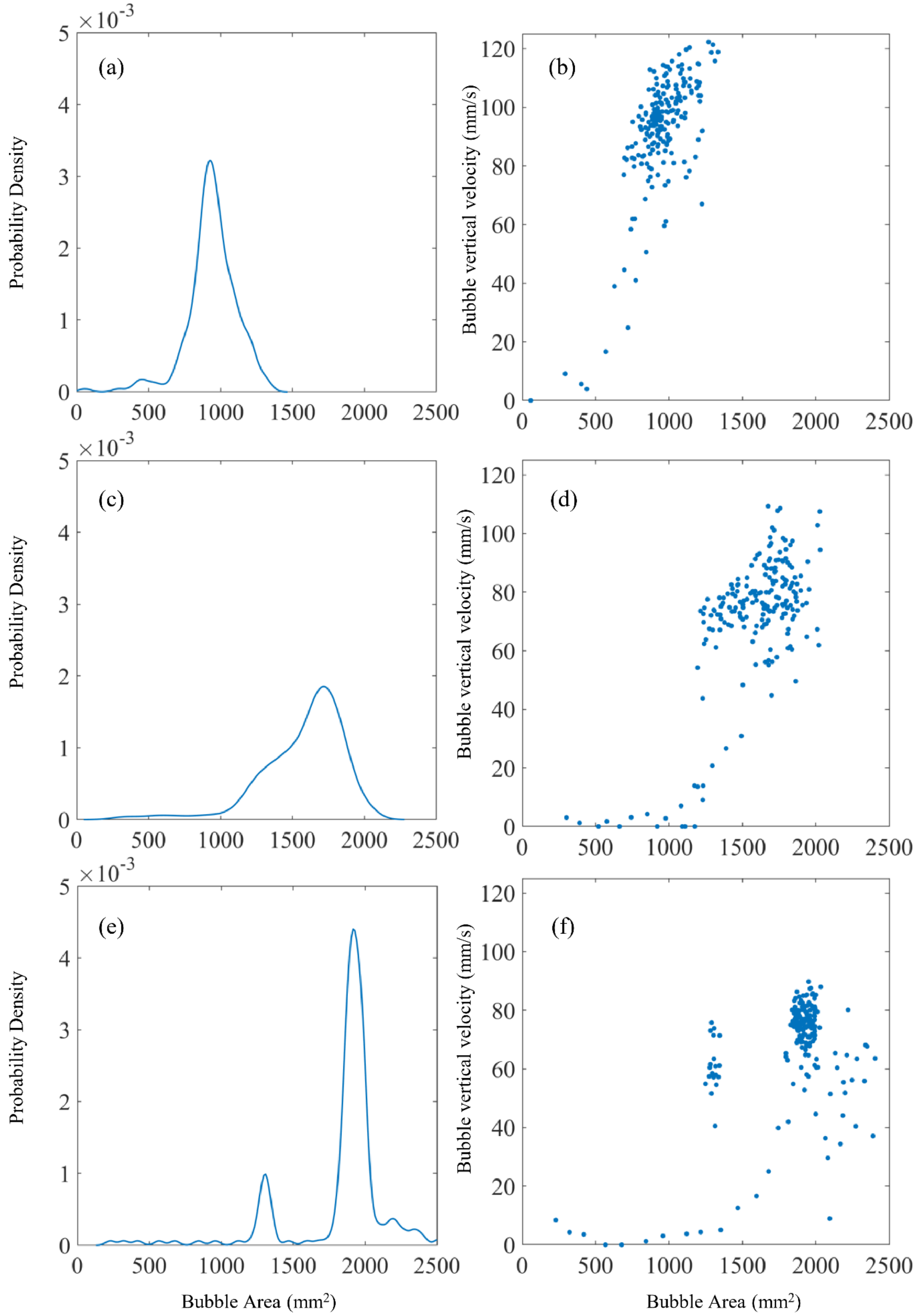

Fig 8. (a,c,e) Probability distribution function of bubble area and (b,d,f) bubble vertical velocity vs. bubble area for the cases with a constant injection time of 160 ms and idle time of 700 ms and seed volume fractions of (a,b) 0%, (c,d) 10%, and (e,f) 20%.

Fig. 9 shows average (a) bubble area and (b) bubble rise velocity vs. vertical position for various particle volume fractions. Experimental results show that the bubble area tends to increase with vertical position due to bubble coalescence. The bubble area sharply increases at vertical positions just below 100 mm in the 20% and 30% cases due to bubbles periodically coalescing just above the injection nozzle in these cases. Bubble rise velocity decreases with increasing volume fraction due to increasing effective suspension velocity. There is a slight increase in bubble rise velocity with increasing vertical position due to bubble size and thus buoyant force increasing. In the case of regular coalescence, we see an increase in the bubble area of approximately 50% after the coalescence (consistent with a doubling of bubble volume which should result in an area increase of 59% for a sphere), but a smaller increase in the velocity of approximately 30%. We attribute this lesser increase in bubble rise velocity as compared to if the system consisted of single bubbles to the effect of bubble interaction. In the region before coalescence, trailing bubbles are accelerated due to wake effects decreasing drag on the trailing bubbles, while after coalescence there are no wake effects to accelerate the merged bubbles. At the location of coalescence, there is an apparent drop in the velocity (**Fig. 9c**) which we attribute to two possible factors, both physical and methodological. A physical cause is the bubbles adjusting in shape towards a more spherical shape directly after coalescing. A newly coalesced bubble will experience more drag force per unit volume than a more spherical bubble developed later, and as such newly coalesced bubbles rise at a slower velocity than a fully developed bubble. In addition, the bubble tracking algorithm is susceptible to artifacts at the moment of coalescence. The algorithm assigns each bubble a unique identifier. During coalescence, sometimes the newly formed bubble is assigned a new identifier, in which case the initial velocity is not recorded, and in other cases it receives the identifier of one of the pre-existing bubbles, more commonly the leading bubble. After coalescence the bubble is larger and has a centroid position between the initial centroid of each of the bubbles before coalescence, which results in an apparent decrease in the centroid location compared to the leading bubble, as can be seen in **Fig. 7** (first column). When averaged together with the rising bubbles, this creates an apparent decrease in rise velocity.

In **Fig. 9**, bubble rise velocities are compared with those predicted for a single bubble rising through a quiescent fluid as predicted by Stokes' Law as well as the theoretical formula obtained by Datta and Srivastava [40] for flow past spheroid objects. Stokes' Law reads : $v = \frac{2}{9}\frac{\Delta\rho g r^2}{\eta}$, where v is the rise velocity, r is the bubble radius taken from the MRI area measurements, $\Delta\rho$ is the difference in density between the bubble and the liquid, g is the acceleration due to gravity, and η is the effective viscosity of the fluid. On the other hand, from

Datta and Srivastava [40] we have $v = (\frac{4}{3}\rho gab^2)/(\frac{16\eta ae^3}{[(1+2e^2)sin^{-1}e-e]})$. This formula modifies the Stokes' equation to account for the role of non-sphericity of the bubbles, written here for an oblate spheroid. a and b are the equatorial radius and the distance from center to the pole along the symmetry axis, respectively. e is the eccentricity of the spheroid defined by $e = \sqrt{1-\frac{b^2}{a^2}}$. We also model the effective viscosity of the suspension as having the form $\eta = \mu(1-\frac{\phi}{\phi_c})^{-2}$ [39], where μ is the dynamic viscosity of the suspending fluid (5.15 Pa s), and ϕ is the volume fraction of seeds. ϕ_c is the maximum random packing fraction, measured using water displacement to be 0.55±0.05 [28], which agrees well with the predicted value of 0.56±0.04 from [39]. Since the observed bubbles in our experiments are not quite spherical and undergo different shape transition before, during and after interactions with one another, it can be observed from **Fig. 9** that the spheroid assumption gives closer velocity approximations than the spherical formula of Stokes velocity.

For cases with 0%, 10% and 20% seed volume fractions, the Datta and Srivastava [40] velocity is fairly close to the experimental velocity. For the 30% and 40% volume fraction cases, the Datta and Srivastava [40] velocity is much lower than the experimental rise velocity, which can be attributed to (i) bubble interaction increasing bubble rise velocity, (ii) the viscosity model over-predicting the effective viscosity for this volume fraction, which is consistent with previous work on these materials [28], and (iii) the particle fraction within the bubble rise column becoming lower than the overall average fraction, leading to the bubble feeling a locally lower effective viscosity. Overall, the results indicate that (i) non-sphericity has a significant effect on bubble rise velocity, (ii) a viscosity model with an exponential value less negative than -2 may be more appropriate for modeling viscosity for this particular suspension and (iii) bubble interaction causes significant deviation from single bubbles in the bubble stream dynamics.

286

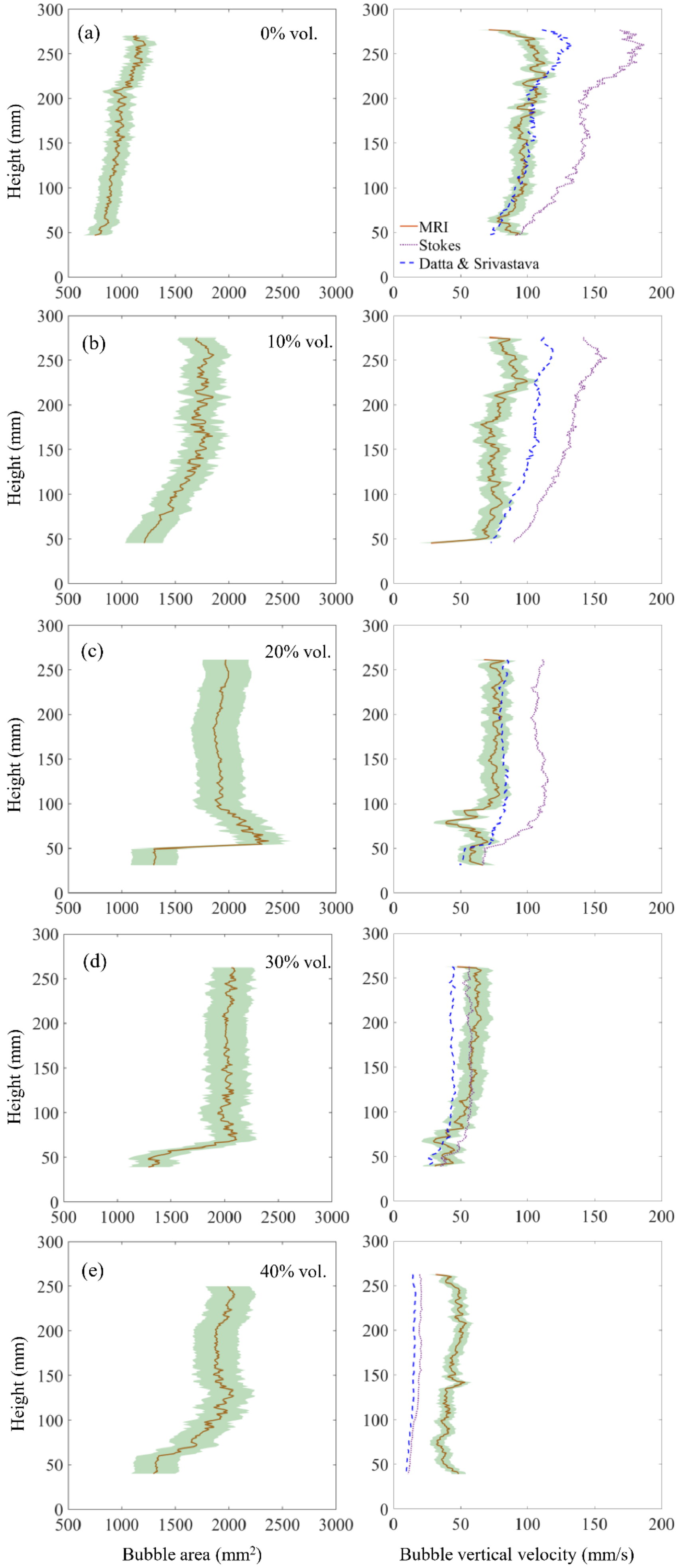
(a)
0% vol.
(b)
10% vol.
(c)
20% vol.
(d)
30% vol.
(e)
40% vol.
Height (mm)
Bubble area (mm²)
Bubble vertical velocity (mm/s)
MRI
Stokes
Datta & Srivastava

Fig. 9 Time-averaged bubble area and bubble rise velocity vs. height for different volume fractions of seeds. Shaded areas show the standard deviation about the mean value. The purple dotted curves represent the Stokes velocity, and the blue dashed line curves show the velocity obtained from Datta and Srivastava [40] formula. These data are for a constant injection time of 160 ms and idle time of 700 ms.

3.2 Varying Idle Time between Injections with 20 vol% Seeds

Fig. 10 shows time series of bubble images from a central vertical slice for different idle times between bubble injections. **Fig. 11** shows the bubble trajectories vs. time and the corresponding bubble area vs. vertical position for the different idle times. For the 700 ms idle time, bubbles coalesce periodically every two bubble injections just above the injection nozzle, as seen in Section 3.1. For the 1050 ms idle time, bubbles do not coalesce until higher in the system and the coalescence events occur at irregular locations and intervals. For the 1400 ms idle time case, bubbles rarely coalesce and only very high above the injection port.

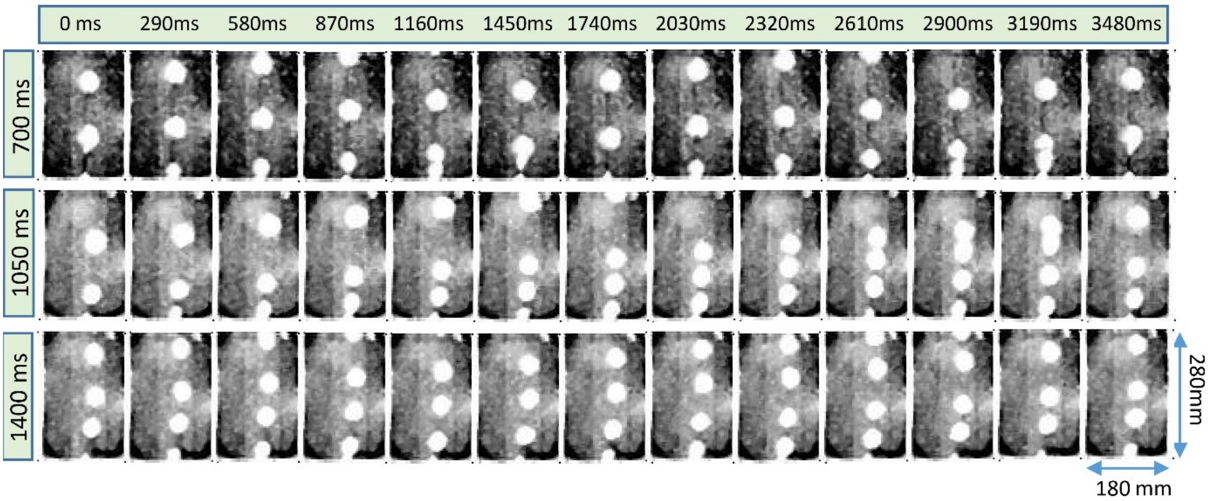

Fig. 10 Time series of 2D central slice images of bubble streams rising through suspensions with idle times of 700 ms (top row), 1050 ms (middle row), and 1400 ms (bottom row) while maintaining a constant injection time of 160 ms through a suspension of 20 vol% seeds. The timestamps are relative to the zero frame chosen for each case; the absolute times of the first tile on each row are 5.9 s, 3.5 s, and 7.2 s, respectively.

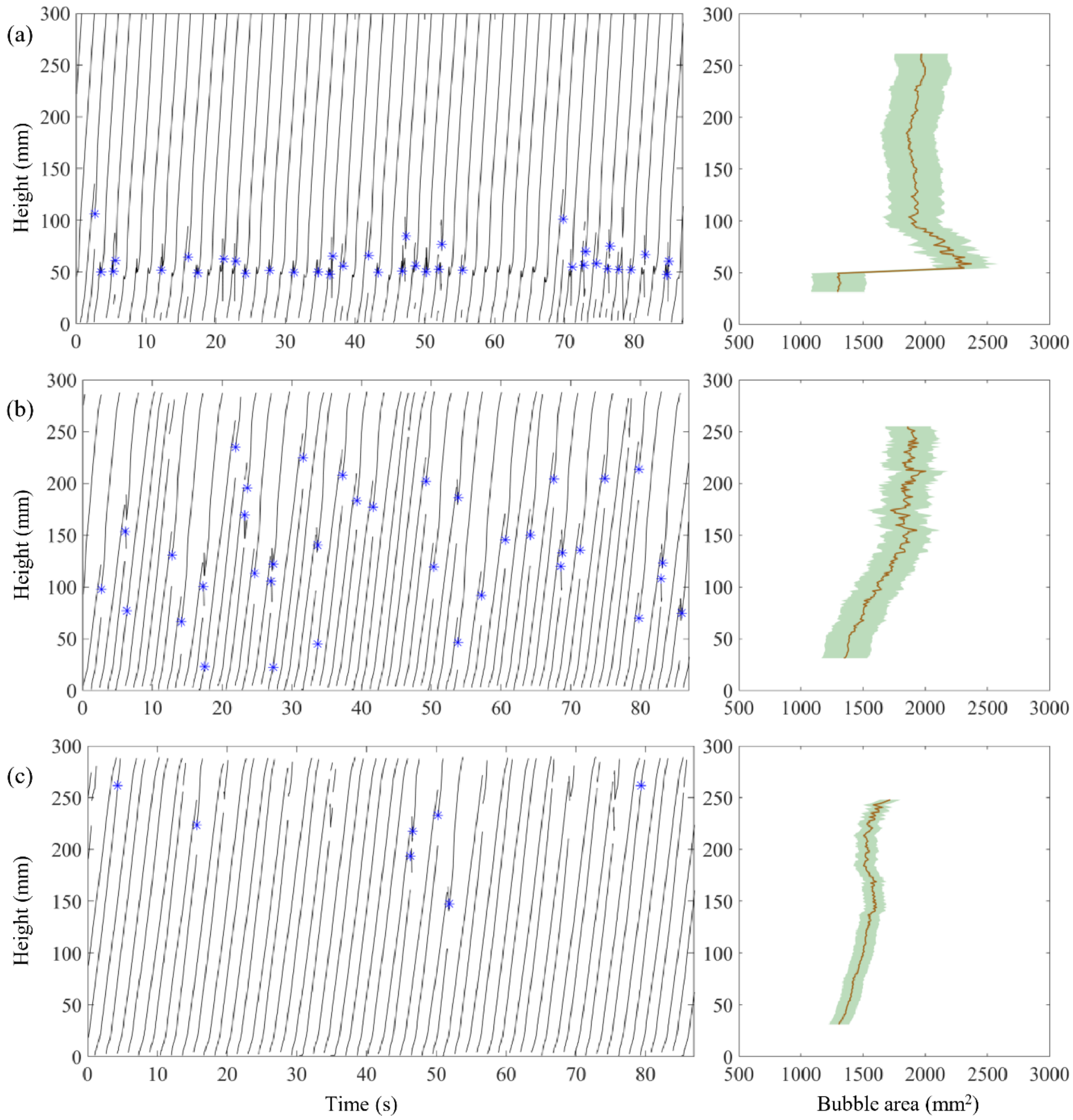

Fig. 11 Vertical bubble position vs. time (left column) and vs. bubble area (right column) with idle times of (a) 700ms, (b) 1050 ms, and (c) 1400 ms. Vol% seeds: 20%; injection time: 160 ms.

Fig. 12 shows (a) bubble area and (b) bubble rise velocity vs. vertical position for 20 vol% cases with different idle times between bubble injections. The bubble area increases sharply in the 700 ms idle time case due to the periodic bubble coalescence, and the bubble area increases steadily with vertical position due to irregular bubble coalescence in the 1050 ms idle time case. In the 1400 ms idle time case, the bubble area only slightly increases with vertical position, likely due to shape relaxation since bubble coalescence occurs only rarely. Bubble rise velocity does not vary significantly with varying vertical position or with varying idle time. Again, we observe that the rise velocities are less sensitive to bubble radius than would be expected for fully isolated bubbles in the lower part of the system in the 700 ms and

1050 ms idle time cases. As the time between bubble injections increases and coalescence becomes less prevalent, the bubble rise velocity is also more consistent through the full height of the system. Consistent with the results in **Fig. 9** and subsequent analysis, the experimental results for bubble rise velocity in Fig. 12 match fairly well with the Datta and Srivastava [40] rise velocity, but are over-predicted by the Stokes rise velocity.

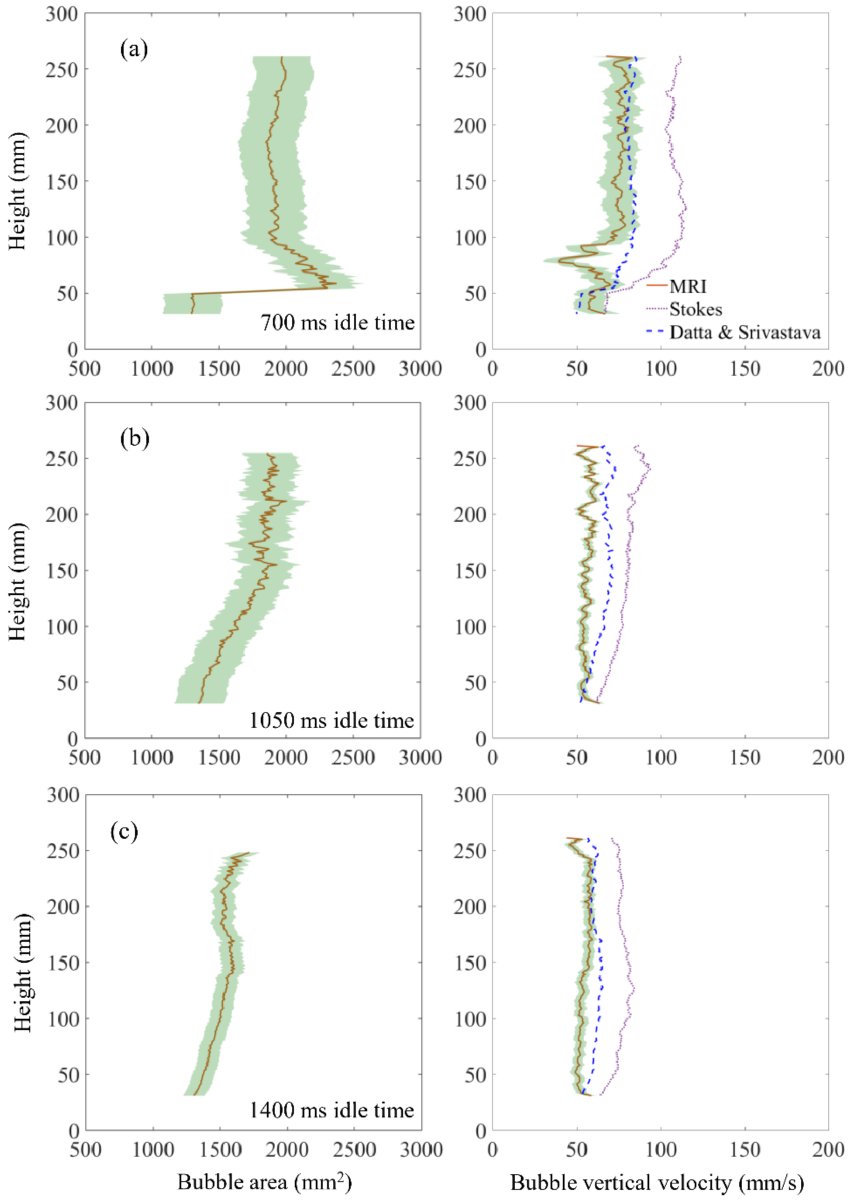

Fig. 12 Time-averaged bubble area and bubble rise velocity vs. height for idle times of (a) 700, (b) 1050, and (c) 1400ms. Shaded areas show the standard deviation about the mean value. The purple dotted curves represent the Stokes velocity, and the blue dashed line curves show the velocity obtained from Datta and Srivastava [40] formula. Injection time: Vol% seeds: 20%; injection time: 160 ms.

3.3 Varying Idle Time between Injection with 40 vol% Seeds

Fig. 13 shows a time series of bubble images with different idle times (different rows) for 40 vol% seeds. These cases differ from the 20 vol% seeds cases above, because the increased concentration of seeds leads to an increase in apparent viscosity, and consequently slower ascent velocities and closer inter-bubble spacing for bubbles of the same size and injection frequency. These conditions promote bubble coalescence. **Fig. 14** shows corresponding bubble trajectories over time (left column) and bubble area vs. vertical position (right column) for the varying idle times (a-c). In the 700 ms idle time case, bubbles coalesce at irregular positions 50-200 mm above the injection port. At certain instants, three bubbles coalesce at once (can be seen at 1740 ms). For the 1400 ms idle time, bubbles coalesce fairly regularly near the injection port and then rarely high up in the system. In the 3500 ms idle time, bubbles never coalesce and instead rise through the system with a steady separation distance between bubbles.

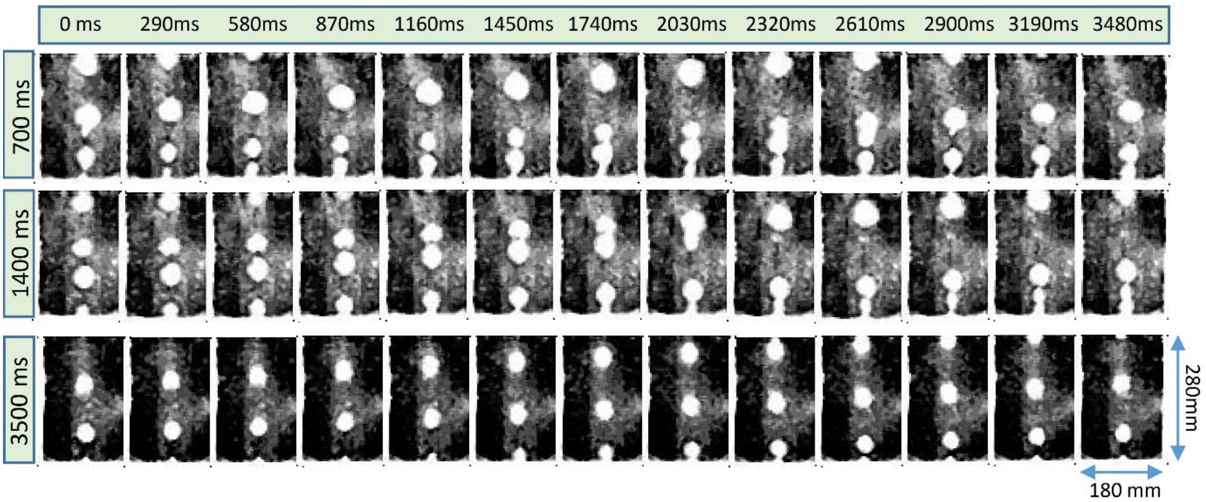

Fig. 13 Time series of 2D images of bubble streams rising through suspensions with different idle times (different rows). Vol% seeds: 40%; injection time: 160 ms. The timestamps are relative to the zero frame chosen for each case; the actual times of the first tile on each row are 80.6 s, 20.4 s, and 7.6 s, respectively.

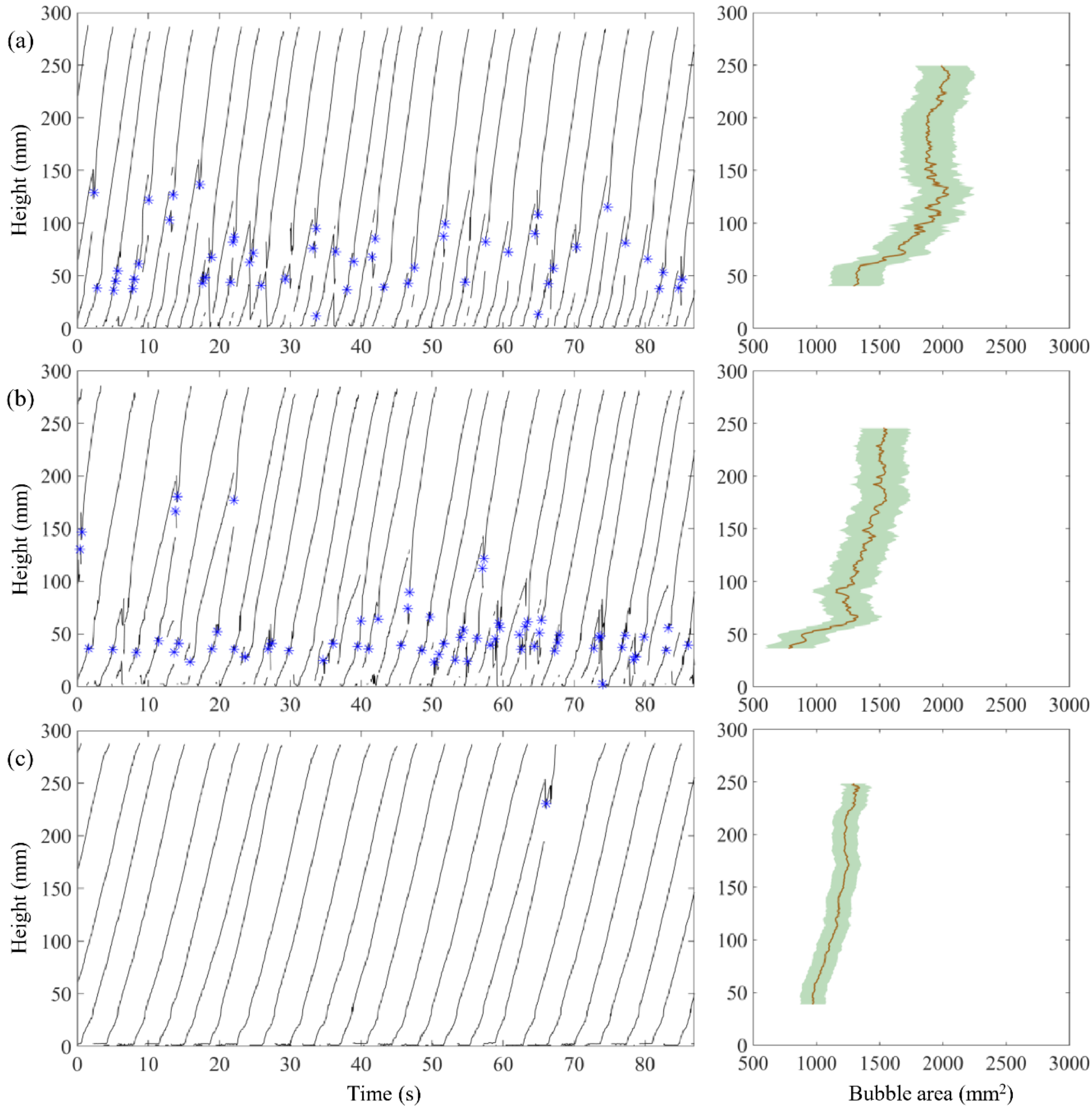

Fig. 14 Representative cases of vertical bubble position vs. time (left column) and vs. bubble area (right column) with idle times of (a) 700 ms, (b) 1400 ms, and (c) 3500 ms. Vol% seeds: 40%; injection time: 160 ms.

Fig. 15 shows (a) bubble area and (b) bubble rise velocity vs. vertical position for various idle times (different columns) in the 40 vol% suspension. With increasing idle time, bubble area and bubble rise velocity decrease due to decreasing amounts of bubble coalescence. In the 3500 ms idle time case, the bubble area only increases slightly with increasing vertical position, perhaps due to changing bubble shape, and bubble rise velocity does not change significantly with vertical position due to the lack of bubble coalescence. For all cases, the bubble rise velocity is much higher than theoretical velocities, which can be attributed to the (i) theory overestimating the effective viscosity of the suspension (discussed further below) and (ii) bubble interaction enhancing the rise velocity of bubbles.

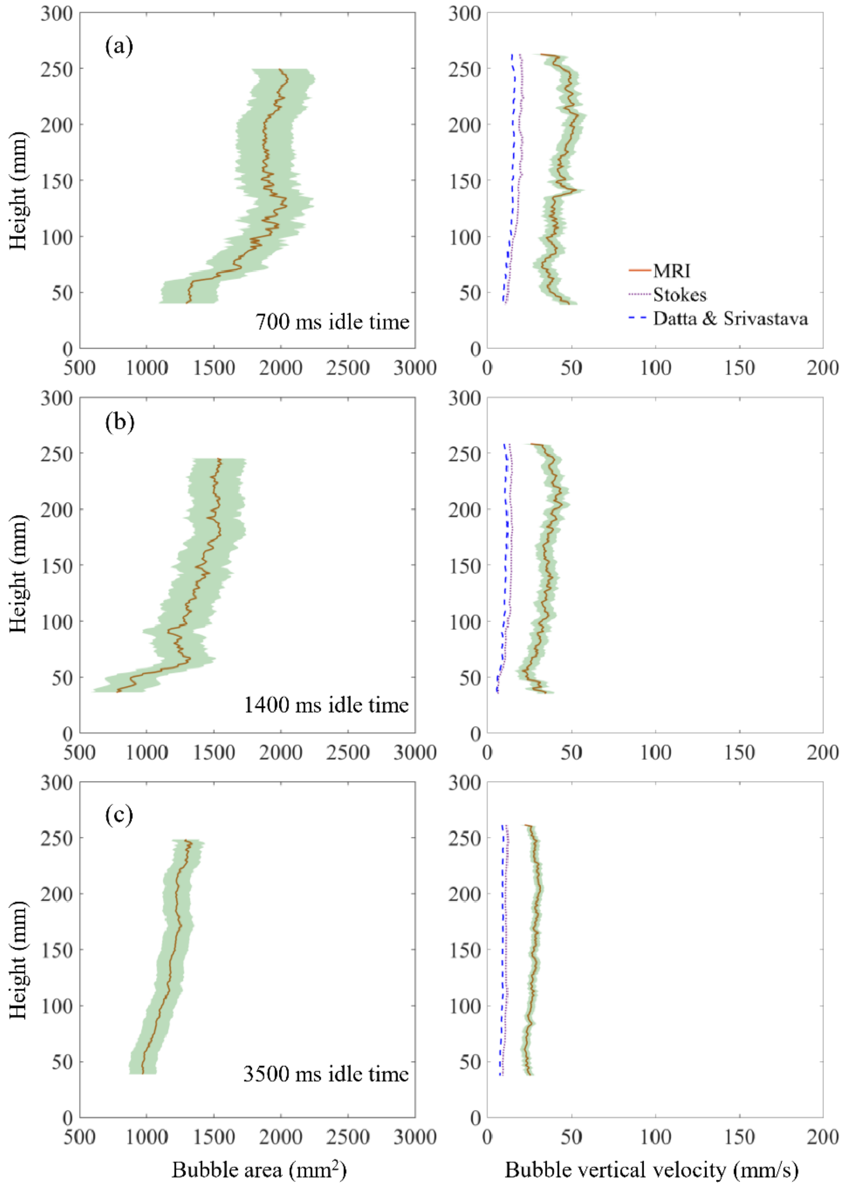

Fig. 15 Time-averaged bubble area and bubble rise velocity vs. height for idle times of (a) 700, (b) 1400, and (c) 3500ms. Shaded areas show the standard deviation about the mean value. The purple dotted curves represent the Stokes velocity, and the blue dashed line curves show the velocity obtained from Datta and Srivastava [40] formula. Injection time: Vol% seeds: 40%; injection time: 160 ms.

From the 3500 ms idle time case, we can evaluate the rise velocity of the bubbles far from the influence of one another. We measure a velocity of 15-25 mm/s for bubbles of radius 13-16 mm. We can rearrange Stokes' law to solve for the apparent viscosity of the suspension and find ~25 Pa s. This value is very low compared to the expected value of 69 $\pm^{60}_{23}$ Pa s based on the suspended volume fraction of particles [28,41]. This may be a result of particle alignment and mixing induced by the repeated bubble injections, which can form lower viscosity pathways and shear bands. This effect is most readily identifiable in the higher concentration suspensions but may be present at even low concentrations as noted in the experiments of [28] using the same materials in a different geometry. This also explains why the experiments in section 3.1 using 30 and 40 vol% seeds are very similar despite the predicted sharp increase in viscosity from $24.9 \pm^{7.3}_{4.3}$ to $69 \pm^{60}_{23}$ Pa s.

4. Conclusion

EPI and MB-EPI were used to characterize the dynamics of bubbles injected periodically into silicone oil-sesame-seed suspensions. MB-EPI produced fully 3D images of the bubble dynamics, but had too low of a signal-to-noise ratio to produce accurate images of bubble dynamics for suspensions over 10% volume fraction seeds. In 10% volume cases, bubbles deviated from axisymmetric conditions at instances surrounding bubble coalescence, which could be attributed to asymmetric particle rearrangements. EPI images were able to characterize bubble dynamics at all volume fractions for 2D slices through the 3D system. Bubble area steadily increased with vertical position in the system in most cases due to bubble coalescence, and in one case, bubbles regularly coalesced at one position in the system. Increasing particle volume fraction tended to increase bubble area since increased effective viscosity acted to slow bubbles, allowing for more bubble coalescence. Increasing idle time between bubble injections caused bubble area to decrease due to fewer coalescence events. In the low particle volume fraction cases, the rise velocity of isolated bubbles agreed with the rise speed predicted by the Datta and Srivastava [40] law for oblate spheroids, but disagreed with Stokes' law for perfect spheres. Rise velocities were larger than those predicted by theory for high volume fraction cases, which was attributed to an overestimation of the effective viscosity by theory due to particle alignment and shear-banding occurring in the experimental conditions here.

Acknowledgements:

This work was funded by a Columbia University Research Initiatives in Science and Engineering grant as well as National Science Foundation grants 2144763, 2024346, and 1929008.

References

[1] M.A. Talaia, Terminal velocity of a bubble rise in a liquid column, World Academy of Science, Engineering and Technology 28 (2007) 264–268.

[2] Y. Li, N. Yang, X. Xiao, B. Jiang, Y. Sun, L. Zhang, Numerical study of the geometric characteristics and kinetic behavior of single bubble rise processes in different liquids, Physics of Fluids 35 (2023).

[3] A. Smolianski, H. Haario, P. Luukka, Vortex shedding behind a rising bubble and two-bubble coalescence: a numerical approach, Applied Mathematical Modelling 29 (2005) 615–632.
[4] X. Luo, J. Zhang, K. Tsuchiya, L.-S. Fan, On the rise velocity of bubbles in liquid-solid suspensions at elevated pressure and temperature, Chemical Engineering Science 52 (1997) 3693–3699.
[5] N. Zhao, B. Wang, Q. Kang, J. Wang, Effects of settling particles on the bubble formation in a gas-liquid-solid flow system studied through a coupled numerical method, Physical Review Fluids 5 (2020) 033602.
[6] P. Luty, M. Prończuk, K. Bizon, Experimental verification of different approaches for the determination of gas bubble equivalent diameter from optical imaging, Chemical Engineering Research and Design 185 (2022) 210–222.
[7] A. Padash, B. Chen, C.M. Boyce, Characterizing alternating bubbles emerging from two interacting vertical gas jets in a liquid, Chemical Engineering Science 248 (2022) 117199.
[8] J. Laverman, X. Fan, A. Ingram, M. van Sint Annaland, D. Parker, J. Seville, J. Kuipers, Experimental study on the influence of bed material on the scaling of solids circulation patterns in 3D bubbling gas–solid fluidized beds of glass and polyethylene using positron emission particle tracking, Powder Technology 224 (2012) 297–305.
[9] V. Verma, J.T. Padding, N.G. Deen, J. Kuipers, F. Barthel, M. Bieberle, M. Wagner, U. Hampel, Bubble dynamics in a 3-D gas–solid fluidized bed using ultrafast electron beam X-ray tomography and two-fluid model, AIChE Journal 60 (2014) 1632–1644.
[10] T. Hensler, M. Tupy, T. Strer, T. Pöschel, K.-E. Wirth, Positron emission particle tracking in fluidized beds with secondary gas injection, Powder Technology 279 (2015) 113–122.
[11] S. Maurer, D. Gschwend, E.C. Wagner, T.J. Schildhauer, J.R. van Ommen, S.M. Biollaz, R.F. Mudde, Correlating bubble size and velocity distribution in bubbling fluidized bed based on X-ray tomography, Chemical Engineering Journal 298 (2016) 17–25.
[12] M. Banowski, M. Beyer, L. Szalinski, D. Lucas, U. Hampel, Comparative study of ultrafast X-ray tomography and wire-mesh sensors for vertical gas–liquid pipe flows, Flow Measurement and Instrumentation 53 (2017) 95–106.
[13] C.M. Boyce, A. Penn, M. Lehnert, K.P. Pruessmann, C.R. Müller, Effect of liquid bridging on bubbles injected into a fluidized bed: A magnetic resonance imaging study, Powder Technology 343 (2019) 813–820.
[14] P. Behruzi, A. Hunt, R. Foster-Turner, Evaluation of liquid sloshing using electrical capacitance tomography, in: AIAA Propulsion and Energy 2020 Forum, 2020: p. 3804.
[15] A.B. Graas, E.C. Wagner, T. van Leeuwen, J.R. van Ommen, K.J. Batenburg, F. Lucka, L.M. Portela, X-ray tomography for fully-3D time-resolved reconstruction of bubbling fluidized beds, Powder Technology 434 (2024) 119269.
[16] D.J. Parker, C.J. Broadbent, P. Fowles, M.R. Hawkesworth, P. McNeil, Positron emission particle tracking-a technique for studying flow within engineering equipment, Nuclear Instruments and Methods in Physics Research Section A: Accelerators, Spectrometers, Detectors and Associated Equipment 326 (1993) 592–607.
[17] P.N. Rowe, B.A. Partridge, An x-ray study of bubbles in fluidised beds, Chemical Engineering Research and Design 75 (1997) S116–S134. https://doi.org/10.1016/S0263-8762(97)80009-3.
[18] M. Pore, G.H. Ong, C.M. Boyce, M. Materazzi, J. Gargiuli, T. Leadbeater, A.J. Sederman, J.S. Dennis, D.J. Holland, A. Ingram, P. Lettieri, D.J. Parker, A comparison of magnetic resonance, X-ray and positron emission particle tracking measurements of a single jet of gas entering a bed of particles, Chemical Engineering Science 122 (2015) 210–218. https://doi.org/10.1016/j.ces.2014.09.029.

[19] A. Penn, T. Tsuji, D.O. Brunner, C.M. Boyce, K.P. Pruessmann, C.R. Müller, Real-time probing of granular dynamics with magnetic resonance, Science Advances 3 (2017) e1701879. https://doi.org/10.1126/sciadv.1701879.
[20] W. Warsito, L.-S. Fan, Measurement of real-time flow structures in gas–liquid and gas–liquid–solid flow systems using electrical capacitance tomography (ECT), Chemical Engineering Science 56 (2001) 6455–6462. https://doi.org/10.1016/S0009-2509(01)00234-2.
[21] R.F. Mudde, Time-resolved X-ray tomography of a fluidized bed, Powder Technology 199 (2010) 55–59. https://doi.org/10.1016/j.powtec.2009.04.021.
[22] A. Eghbalmanesh, N. Romijn, M.W. Baltussen, E.A.J.F. (Frank) Peters, K.A. Buist, J. a. M. Kuipers, Hydrodynamics in a randomly packed bed of spheres: A comparison between PR-CFD simulations and MRI experiments, AIChE Journal n/a (n.d.) e18322. https://doi.org/10.1002/aic.18322.
[23] T. Pavlin, R. Wang, R. McGorty, M.S. Rosen, D.G. Cory, D. Candela, R.W. Mair, R.L. Walsworth, Noninvasive Measurements of Gas Exchange in a Three-Dimensional Fluidized Bed by Hyperpolarized 129Xe NMR, Appl Magn Reson 32 (2007) 93–112. https://doi.org/10.1007/s00723-007-0002-7.
[24] H.T. Fabich, A.J. Sederman, D.J. Holland, Study of bubble dynamics in gas-solid fluidized beds using ultrashort echo time (UTE) magnetic resonance imaging (MRI), Chemical Engineering Science 172 (2017) 476–486.
[25] M. Errigo, C. Windows-Yule, M. Materazzi, D. Werner, P. Lettieri, Non-invasive and non-intrusive diagnostic techniques for gas-solid fluidized beds – A review, Powder Technology 431 (2024) 119098. https://doi.org/10.1016/j.powtec.2023.119098.
[26] J.D. Seymour, A. Caprihan, S.A. Altobelli, E. Fukushima, Pulsed Gradient Spin Echo Nuclear Magnetic Resonance Imaging of Diffusion in Granular Flow, Phys. Rev. Lett. 84 (2000) 266–269. https://doi.org/10.1103/PhysRevLett.84.266.
[27] C.M. Boyce, A. Penn, M. Lehnert, K.P. Pruessmann, C.R. Müller, Wake volume of injected bubbles in fluidized beds: A magnetic resonance imaging velocimetry study, Powder Technology 357 (2019) 428–435.
[28] J. Birnbaum, W. Zia, A. Bordbar, R.F. Lee, C.M. Boyce, E. Lev, Magnetic resonance imaging of multi-phase lava flow analogs: Velocity and rheology, Journal of Geophysical Research: Solid Earth (2023) e2023JB026464.
[29] A. Penn, T. Tsuji, D.O. Brunner, C.M. Boyce, K.P. Pruessmann, C.R. Müller, Real-time probing of granular dynamics with magnetic resonance, Science Advances 3 (2017) e1701879.
[30] L.F. Gladden, L.D. Anadon, C.P. Dunckley, M.D. Mantle, A.J. Sederman, Insights into gas–liquid–solid reactors obtained by magnetic resonance imaging, Chemical Engineering Science 62 (2007) 6969–6977.
[31] C.R. Müller, D.J. Holland, A.J. Sederman, M.D. Mantle, L.F. Gladden, J.F. Davidson, Magnetic resonance imaging of fluidized beds, Powder Technology 183 (2008) 53–62.
[32] D.J. Larkman, J.V. Hajnal, A.H. Herlihy, G.A. Coutts, I.R. Young, G. Ehnholm, Use of multicoil arrays for separation of signal from multiple slices simultaneously excited, Journal of Magnetic Resonance Imaging 13 (2000) 313–317. https://doi.org/10.1002/1522-2586(200102)13:2%3C313::AID-JMRI1045%3E3.0.CO;2-W.
[33] M.K. Stehling, R. Turner, P. Mansfield, Echo-Planar Imaging: Magnetic Resonance Imaging in a Fraction of a Second, Science 254 (1991) 43–50.
[34] P.T. Callaghan, Principles of nuclear magnetic resonance microscopy, Oxford Unveristy Press, 1991.
[35] P. Parasoglou, D. Malioutov, A.J. Sederman, J. Rasburn, H. Powell, L.F. Gladden, A. Blake, M.L. Johns, Quantitative single point imaging with compressed sensing, Journal of Magnetic Resonance 201 (2009) 72–80. https://doi.org/10.1016/j.jmr.2009.08.003.

[36] A. Haase, J. Frahm, D. Matthaei, W. Hanicke, K.-D. Merboldt, FLASH imaging. Rapid NMR imaging using low flip-angle pulses, Journal of Magnetic Resonance (1969) 67 (1986) 258–266. https://doi.org/10.1016/0022-2364(86)90433-6.
[37] D.A. Feinberg, S. Moeller, S.M. Smith, E. Auerbach, S. Ramanna, M.F. Glasser, K.L. Miller, K. Ugurbil, E. Yacoub, Multiplexed echo planar imaging for sub-second whole brain FMRI and fast diffusion imaging, PloS One 5 (2010) e15710.
[38] A. Fedorov, R. Beichel, J. Kalpathy-Cramer, J. Finet, J.-C. Fillion-Robin, S. Pujol, C. Bauer, D. Jennings, F. Fennessy, M. Sonka, 3D Slicer as an image computing platform for the Quantitative Imaging Network, Magnetic Resonance Imaging 30 (2012) 1323–1341.
[39] S. Mueller, E. Llewellin, H. Mader, The effect of particle shape on suspension viscosity and implications for magmatic flows, Geophysical Research Letters 38 (2011).
[40] S. Datta, D.K. Srivastava, Stokes drag on axially symmetric bodies: a new approach, Proceedings-Mathematical Sciences 109 (1999) 441–452.
[41] R. Roscoe, The viscosity of suspensions of rigid spheres, British Journal of Applied Physics 3 (1952) 267.